Nuclear Inst. and Methods in Physics Research, A 977 (2020) 164284

Contents lists available at ScienceDirect

Nuclear Inst. and Methods in Physics Research, A

journal homepage: www.elsevier.com/locate/nima

New segmented target for studies of neutron unbound systems

T. Redpath [a,b,*], T. Baumann [a], J. Brown [c], D. Chrisman [a,b], P.A. DeYoung [d], N. Frank [e], P. Guèye [a,b], A.N. Kuchera [f], H. Liu [a,b], C. Persch [d], S. Stephenson [g], K. Stiefel [a,h], M. Thoennessen [a,b,1], D. Votaw [a,b]

[a] National Superconducting Cyclotron Laboratory, Michigan State University, East Lansing, MI 48824, USA
[b] Department of Physics and Astronomy, Michigan State University, East Lansing, MI 48824, USA
[c] Department of Physics, Wabash College, Crawfordsville, IN 47933, USA
[d] Department of Physics, Hope College Holland, Michigan 49422-9000, USA
[e] Department of Physics and Astronomy, Augustana College, Rock Island, IL 61201, USA
[f] Department of Physics, Davidson College, Davidson, NC 28035, USA
[g] Department of Physics, Gettysburg College, Gettysburg, PA 17325, USA
[h] Department of Chemistry, Michigan State University, East Lansing, MI, 48824, USA

ARTICLE INFO

Keywords:
Invariant mass spectroscopy
Silicon detectors
Reaction yield
Neutron drip line
Radioactive ion beam
Half-life

ABSTRACT

The study of neutron-unbound systems using invariant mass spectroscopy is often performed using low-intensity radioactive ion beams. Low reaction yields can be countered by using thick targets but at the expense of larger uncertainties in the reconstructed invariant mass. We present a new segmented target designed to address this trade-off. It is composed of three ~4 mm thick passive beryllium targets interleaved between four 140 μm thick position sensitive silicon detectors. In the first experiment to use this new system the half-life of two-neutron unbound ^{26}O was measured to be $T_{1/2} = 5.0^{+1.7}_{-2.2}$ (stat)±1.7 (syst) ps, which agrees with a previous measurement made by the MoNA Collaboration.

1. Introduction

1.1. Invariant mass spectroscopy to study neutron-unbound systems

Invariant mass spectroscopy is a well-established experimental technique that can be used to extract nuclear structure information [1,2]. This technique has been applied to study neutron-unbound systems [3]. These experiments provide information about neutron-unbound states that decay on timescales of $\sim 10^{-21}$ s by measuring the energies and momenta of the daughter particles (a charged fragment and one or more neutrons) [4–6].

One kind of experimental setup used to study neutron-unbound states is exemplified by the MoNA-LISA-Sweeper setup at NSCL/MSU [7]. This setup involves a reaction target in which the nuclide of interest is produced, a set of neutron detectors, a dipole magnet and a suite of charged particle detectors. The neutron four-vector is obtained from measuring the time-of-flight (ToF) and the interaction point in the neutron detector. The dipole magnet sweeps charged fragments out of the neutron flight path, and measurements made with the charged particle detectors are used to identify the decay daughter and reconstruct its four-vector. For the case of two-neutron emission, the four-vectors of the daughter fragment and neutrons are then used to calculate the invariant mass M of the short-lived nucleus according to Eq. (1)

$$M^2 = M_A^2 + 2m_N^2 + 2(E_2^2 - \vec{p}_2^2) \tag{1}$$

where

$$E_2^2 = E_A E_{n1} + E_A E_{n2} + E_{n1} E_{n2}$$
$$\vec{p}_2^2 = \vec{p}_A \cdot \vec{p}_{n1} + \vec{p}_A \cdot \vec{p}_{n2} + \vec{p}_{n1} \cdot \vec{p}_{n2}$$

where M_A, E_A and $\vec{p}_A$ (m_N, E_{n1}, E_{n2}, $\vec{p}_{n1}$ and $\vec{p}_{n2}$) are the rest mass, energy and momentum vector of the charged fragment (two neutrons), respectively. The difference between the invariant masses of the parent and daughter particles is defined as the decay energy, see Eq. (2), and corresponds to the excitation energy in the unbound parent system above the neutron emission threshold.

$$E_{\text{decay}} = \sqrt{M_A^2 + 2m_N^2 + 2(E_2^2 - \vec{p}_2^2)} - M_A - 2m_N \tag{2}$$

1.2. Decay energy reconstruction

Reconstructing the decay energy requires knowledge of the fragment and neutron four-vectors at the decay vertex inside the target

* Corresponding author at: National Superconducting Cyclotron Laboratory, Michigan State University, East Lansing, MI 48824, USA.
E-mail address: redpath@nscl.msu.edu (T. Redpath).
[1] Present address: American Physical Society, Ridge, NY 11961, USA.

https://doi.org/10.1016/j.nima.2020.164284
Received 5 December 2019; Received in revised form 26 April 2020; Accepted 16 June 2020
Available online 29 June 2020

material. The material between the decay vertex and the neutron detectors induces a negligible amount of scattering for the neutrons, so the time-of-flight and position measurements reliably capture the neutron information needed for the decay energy calculation. Recovery of the fragment energy and momentum at the decay vertex is more challenging because the location of the decay is not measured. Therefore, the energy lost as the fragment moves through the remainder of the target material must be estimated and added to the fragment momentum measured after the target. The energy loss estimate introduces a ∼6% uncertainty in the reconstructed fragment kinetic energy for a 700 mg/cm^2 beryllium target and a beam energy of 105 MeV/u.

1.3. Balancing reaction yield and resolution

Invariant mass spectroscopy experiments to study neutron-unbound states are based on radioactive ion beams (RIBs) produced via in-flight projectile fragmentation. The intensity of the fragment beam can range from ∼10–1000 particles/s [8,9]. The beam is then directed onto the reaction target. Typical cross-sections for the one- or two-proton knockout reactions commonly used in studies of neutron-unbound systems are ∼1 mb and ∼0.1 mb, respectively [3]. Thus experiments at the limit of feasibility would greatly benefit from any method that increases reaction yield.

One way to increase reaction yield is to use a thick target to increase the number density of target nuclei. This approach negatively impacts the resolution of the decay energy measurement. For example, the 6% uncertainty discussed previously for a 700 mg/cm^2 is inflated to 42% for a 2100 mg/cm^2 beryllium target.

An active target could directly measure the energy loss event-by-event. In current active target systems, the fill gas acts as both the target and detector material [10–13]. To produce the same reaction rate as a 1 cm thick solid beryllium target, an active target filled with an ideal gas would need to be 10^7 m long and operate at 500 kPa (∼5 atm). This estimate assumes identical reaction cross-sections for beryllium and the ideal gas.

A compact solution is a system composed of multiple solid, thin targets interleaved with energy loss detectors. This system localizes the decay position to one of the target sections and this reduces the uncertainty introduced into the fragment kinetic energy reconstruction. When silicon detectors are used to measure the energy loss, the incident beam rate is limited to ∼1000 particles per second to avoid pileup and excessive radiation damage.

In summary, segmenting a single thick solid target offers improved energy resolution because the decay position can be better localized so that the energy loss needed to reconstruct the fragment momentum at the decay vertex is better approximated.

2. Description of the segmented target/detector system

2.1. Silicon detectors and beryllium targets

The segmented target is a compact multi-layer system consisting of four position-sensitive silicon detectors and three beryllium targets. A schematic depiction is shown in Fig. 1 and a design drawing is shown in Fig. 2. Each silicon detector is a 62 mm × 62 mm ×140 μm phosphorus-doped n-type silicon wafer manufactured by Micron (model MSPSD TL 63) and similar to the detectors described in Ref. [14]. The front face is a boron-implanted p-type layer resistive anode and is bordered by 0.5 mm resistive ion-implanted strips. The resistances between adjacent corners is ∼5.6 kΩ. Aluminum contacts at each corner provide electrical connections that read out the four signals used to reconstruct the interaction position. A fifth signal (referred to as the anode) is taken from the rear face non-resistive layer via an aluminum-evaporated contact to provide an independent measurement of the total energy deposited.

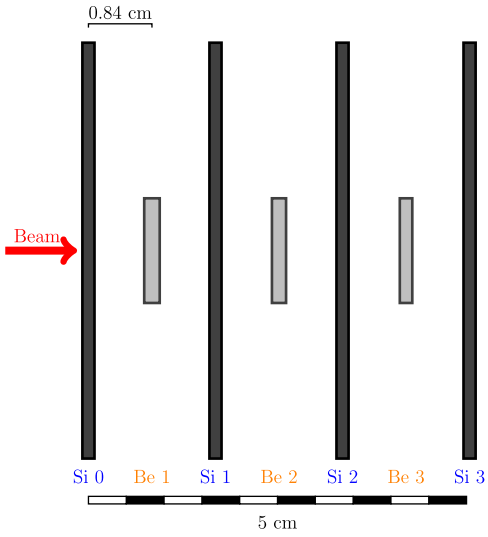

Fig. 1. A schematic drawing of the segmented target. Each detector is 11 cm × 11 cm × 0.32 cm including the frame housing the silicon wafer. The thicknesses of the silicon wafers are 140, 135, 138, 142 μm for detectors 0, 1, 2, 3 respectively. The beryllium targets are 2.8 cm tall with thicknesses of 0.41, 0.37, 0.33 cm for targets 1, 2, 3 respectively. The spacing between each detector/target is 0.84 cm so in total the apparatus extends 5.04 cm along the beam axis.

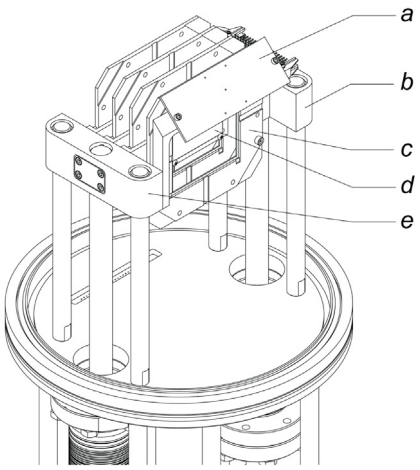

Fig. 2. Design drawing of the segmented target mounted in the beamline: (a) beam viewer plate used to image the beam during tuning (b) base on which all detectors are mounted (c) silicon detector frame (d) beryllium target (e) base on which all targets are mounted. The viewer is mounted to the target base. Both the detector and target mount bases are attached to pneumatic drives so they can be individually inserted into and retracted from the beamline.

The thicknesses of the three beryllium targets are chosen to optimize the production rate of the nucleus of interest and decay energy resolution. The four detectors and three targets are interleaved so that each target sits between two detectors (see Fig. 2). The detectors and target are mounted on two separate pneumatic drive systems that are controlled remotely and can independently drive the detectors and targets in and out of the beam line. The thicknesses of the detectors and targets are listed in Table 1.

2.2. Signal readout and electronics

The four silicon detectors generate 20 signals consisting of 16 corner signals and 4 anode signals. The size of the anode signals are proportional to the total amount of energy deposited in the detector. Each anode signal is DC coupled to a charge-sensitive preamplifier that

Table 1
Thicknesses for the silicon detectors and beryllium targets. The beryllium targets were measured directly using a dial indicator and the associated measurement uncertainties are ±4 μm (±0.7 mg/cm^2 Be). The silicon wafer thicknesses were reported by the manufacturer with uncertainties of ±1 μm (±0.2 mg/cm^2 Si).

Segment	Thickness [μm]	Area density [mg/cm^2]
Si 0	140	32.5
Be 1	4100	758.5
Si 1	135	31.3
Be 2	3736	691.2
Si 2	138	32.0
Be 3	3302	610.9
Si 3	142	33.0

has a typical output signal around 30 mV with a 0.05 μs rise time and a 500 μs fall time when a 5.5 MeV α source is placed 7.1 cm in front of the detector under vacuum. The rise and fall time variations for different incident particles was not studied as part of this work. Each anode signal is then routed to a Tennelec 241S shaping amplifier with a shaping time of 6 μs. The shaped anode signals are routed to a Mesytec MADC-32 analog-to-digital converter with a 4 V range.

The corner signals can be used to reconstruct the position at which the charged particle interacted with the detector [14]. Each corner signal is DC coupled to one of 16 Mesytec MMPR1 preamplifiers. In order to extract a signal, each corner contact is floated above ground by a 10 kΩ resistor on the PCB. The corner signals are some fraction of the anode signal depending on the interaction location of the passing ion. The preamplifier outputs are connected to a single 16-channel Mesytec MSCF-16 shaping amplifier. The shaping time is 2 μs for all corner channels. The shaped signals are routed to a bank of 16 inputs on the same MADC-32 that receives the anode signals.

2.3. MoNA-LISA-Sweeper

The generic setup described in Section 1.1 is implemented at the National Superconducting Cyclotron Laboratory (NSCL) [15] using the MoNA/LISA neutron detectors [16,17] and the Sweeper magnet [18] arranged as shown in Fig. 3. Upon entering the experimental area, the beam first passes through a plastic timing scintillator before impinging on the target where a nuclear reaction (typically one- or multi-nucleon knockout) populates a neutron unbound state that immediately decays to a charged fragment and one or more neutrons. Reaction products and the unreacted beam are then deflected by the Sweeper magnet into a suite of charged particle detectors that consists of two Cathode Readout Drift Chambers (CRDCs) to measure their positions, an ion chamber to measure energy loss for element identification and a large-area thin timing scintillator to measure energy loss and time-of-flight relative to the target timing scintillator mentioned previously. The neutrons are unaffected by the magnetic field and continue on to the neutron detectors that measure time-of-flight relative to the target scintillator as well as position. For the experiment described here, MoNA-LISA consisted of 272 BC-408 and EJ-200 plastic scintillator bars with dimensions 10 × 10 × 200 cm^3 stacked in 17 walls with 16 bars per wall.

2.4. First experiment

The segmented target was first used in an experiment to measure the ground state resonance of ^{26}O with the MoNA/LISA/Sweeper setup (see Fig. 3 and Section 2.3) at the NSCL. The Coupled Cyclotron facility [20] produced a 140 MeV/u ^{48}Ca primary beam that impinged on a 775 mg/cm^2 beryllium production target to produce a ^{27}F secondary beam via in-flight projectile fragmentation. The ^{27}F secondary beam was filtered out from other projectile fragmentation products according to its magnetic rigidity using the A1900 Fragment Separator [21]. An achromatic 450 mg/cm^2 aluminum wedge degrader was placed at the dispersive intermediate image of the A1900 to achieve isotopic separation of the secondary ^{27}F beam. The purity of the ^{27}F beam was 15%. There were three major contaminants ^{28}Ne, ^{29}Ne, and ^{30}Na as well as a number of lighter nuclei including four isotopes of oxygen (^{21}O, ^{22}O, ^{23}O, ^{24}O). These contaminant beams, as well as unreacted ^{27}F, were used to calibrate the energy loss measurements of the silicon detectors as described in Section 3.1.

The ^{27}F secondary beam was directed onto the segmented target to produce ^{26}O via one-proton knockout; ^{24}O reaction fragments were measured in coincidence with neutrons to reconstruct the decay energy spectrum of ^{26}O. The average ^{27}F production rate on target was 17 particles per second producing 2712 measured coincidences between ^{24}O and at least one neutron. The fragment energies were calculated using the time-of-flight measured between the target scintillator and the thin scintillator. Usually fragment kinetic energies are calculated based on the position measurements in the dispersive plane of the Sweeper magnet, but this option was not available due to a malfunction in one of the position-sensitive detectors.

3. Methods

3.1. Energy loss calibration

From the data recorded during the experiment described in Section 2.4, a total of eight different beam fragments were identified with energy losses in the same range (5 MeV–30 MeV) as the energy losses of the ^{27}F($-1p$) reaction products. They are listed in Table 2 along with their kinetic energies determined by the settings of the A1900 fragment separator [21] used to filter and deliver the beam. The kinetic energies of the incoming beam fragments together with the silicon and beryllium thicknesses were used to calculate an expected energy loss for each silicon detector using the ATIMA energy loss calculator embedded in LISE^{++} [22] (see Table 2). The results of these calculations were then plotted against the means extracted from Gaussian fits to the uncalibrated ADC spectra from each silicon detector (see Fig. 4). Parameters p_0 and p_1 for the calibration $dE_{\mathrm{cal}} = p_0 + p_1 \times dE_{\mathrm{raw}}$ were extracted from fits to the plots shown in Fig. 4. The root mean square errors for the fits are 0.13, 0.11, 0.12, and 0.16 MeV for detectors 0, 1, 2, and 3, respectively. Ultimately, a precise energy loss calibration is not necessary for these detectors since their primary function is to separate incoming beam fragments from fragments produced in some type of knockout reaction. This will be discussed in the next section.

The position sensitivity of the detectors was not utilized for the current analysis, however, a preliminary estimation of the position resolution yielded a value $\sim 1.8 \pm 0.1$ mm (FWHM). This is higher than the results found in [14] for in-beam tests of similar detectors. Dependence of the anode signal on position was observed, but this did not obfuscate the target identification procedure described in Section 3.2. This is because the size of the beam spot was smaller than the size of the detectors, ~4 cm^2 compared to 36 cm^2.

3.2. Identifying the reaction target

The first experiment to use the segmented target was described in Section 2.4. Events in which the incoming fragment was ^{27}F are identified via energy loss measured in the first silicon detector and time-of-flight (ToF) from the A1900 to the target scintillator. Events in which a reaction in one of the beryllium targets produced an oxygen isotope are identified from the energy loss measured in the ion chamber after the Sweeper magnet and the ToF from the target scintillator to the thin scintillator. This set of analysis gates selects a subset of events in which a one-proton knockout reaction occurred. To determine if a particular beryllium target induced the proton knockout, the energy loss measured in the upstream silicon detector must be compared to the energy loss measured in the downstream silicon detector. Consider two cases where (1) a nuclear interaction somewhere in the beryllium target

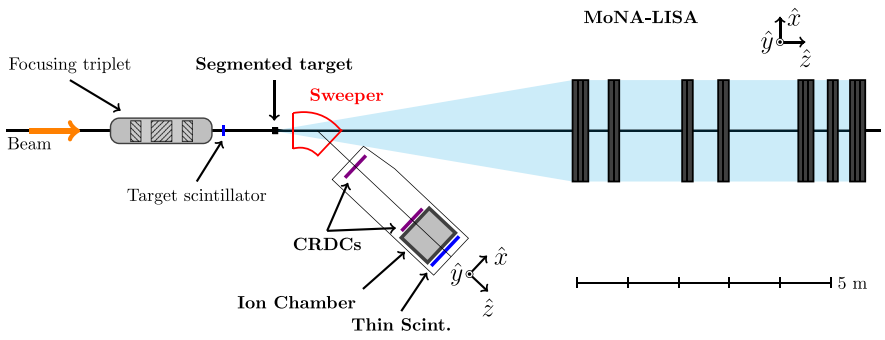

Fig. 3. Detector configuration used at the NSCL for the first experiment with the segmented target [19].

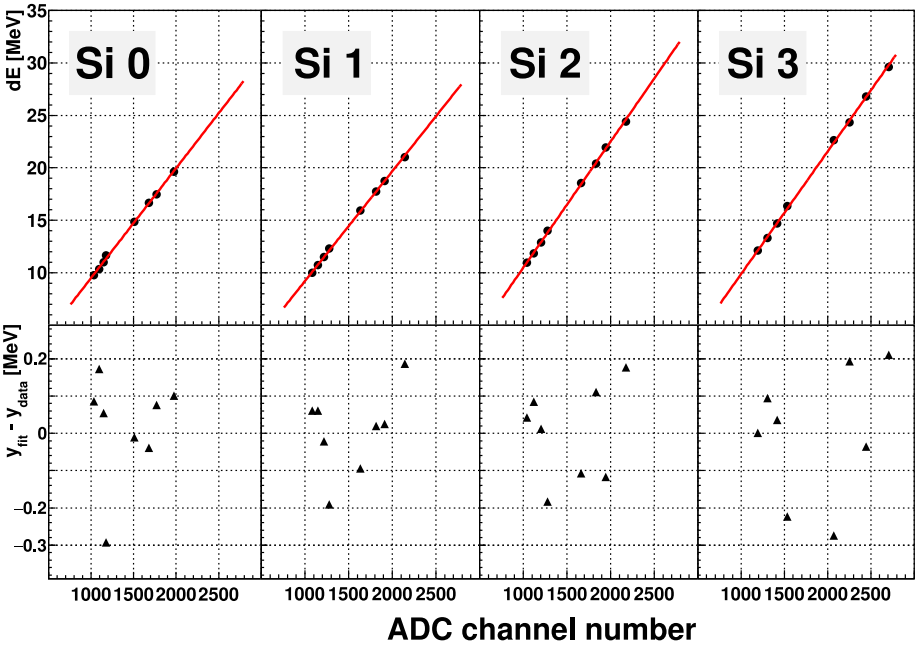

Fig. 4. Black points plot calculated energy loss (y-axis) as a function of fitted centroid of the uncalibrated dE spectrum (x-axis) for eight different beam fragments. The four upper panels show the results for the four silicon detectors. The red lines show the extracted linear fits. The x error bars for the fit errors and the y error bars for the measurement/calculation uncertainties are smaller than the points. The parameters from the fit are listed in Table 3. The deviation of the data points from the fit for each detector is plotted in the lower set of four panels. The RMS errors are 0.13, 0.11, 0.12, and 0.16 MeV for detectors 0, 1, 2, and 3, respectively.

Table 2
Energy loss of eight different fragments in each silicon detector calculated using the ATIMA energy loss calculator included within the LISE^{++} software package [22]. Calculation of these values accounts for the energy loss in the beryllium segments since the targets were always in the beam line. Variations in the material thicknesses correspond to variations in the calculated dE less than ±0.008 MeV, so $\lesssim$0.05%, which is smaller than the resolution of the detectors.

		Energy loss [MeV]			
Fragment	KE [MeV/u]	Si 0	Si 1	Si 2	Si 3
^{21}O	136.8	9.748	10.000	10.946	12.122
^{22}O	125.3	10.345	10.719	11.863	13.316
^{23}O	115.2	10.978	11.485	12.889	14.707
^{24}O	106.3	11.650	12.298	14.004	16.358
^{27}F	105.3	14.838	15.919	18.568	22.649
^{28}Ne	120.2	16.667	17.732	20.393	24.315
^{29}Ne	112.8	17.470	18.747	21.939	26.785
^{30}Na	124.9	19.626	21.006	24.427	29.619

knocks a proton out of ^{27}F and (2) no proton is knocked out: in both cases the energy loss registered by the upstream detector is the same while the downstream detector will record a smaller energy loss in case (1) than it will in case (2) because Z changes from nine to eight and energy loss is proportional to Z^2. Protons from the knockout reactions

Table 3
The second and third columns list parameter values extracted from the fits $dE_{\text{cal}} = p_0 + p_1 dE_{\text{raw}}$, see Fig. 4. The fit errors are <2.0% in the range from 10 MeV to 35 MeV.

Silicon detector	Slope (p_0) [MeV/ADC ch]	Offset (p_1) [MeV]
0	0.0104(1)	−0.86(2)
1	0.0104(1)	−0.99(2)
2	0.0120(1)	−1.30(2)
3	0.0117(1)	−1.52(2)

were estimated to deposit less than 300 keV in any subsequent silicon detector. This is below the sensitivity of these detectors.

Fig. 5 illustrates how the reaction target is identified using the energy loss measurements from the silicon detectors. All events plotted in Fig. 5 are selected so that the incoming fragment was ^{27}F and the outgoing fragment (after the segmented target) was an oxygen isotope. The top row plots the dE spectra for each silicon detector. The bottom row plots the energy loss measured in one detector versus the energy loss measured in the previous detector; spectra in the top row are 1D projections onto the x and y axes of the bottom row plots. The 1D spectra titled "Si 0 dE" is the x-axis of the left-most plot in the bottom row. Si 1 dE is the y-axis on the left-most and the x-axis on the middle

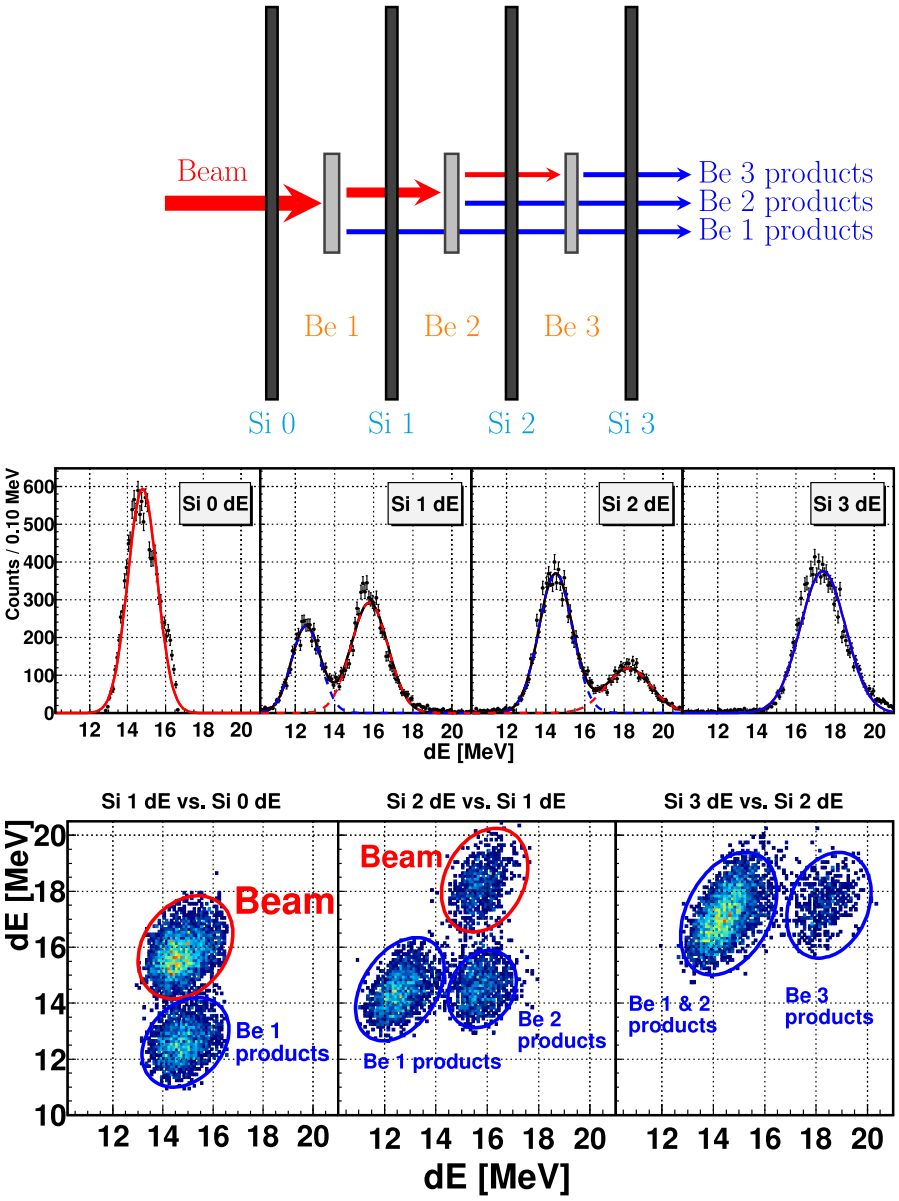

Fig. 5. Example target identification plots for $^{27}\mathrm{F}(-1p) \rightarrow {}^{A}\mathrm{O}$ meaning that all events plotted here enter the segmented target as $^{27}\mathrm{F}$ and leave as an oxygen isotope. The top row of plots show the measured energy loss in each silicon detector. The left panel in the bottom row shows the measured energy loss in the second silicon detector vs. the measured energy loss in the first silicon. The middle panel plots the third silicon energy loss vs. the second and the right panel shows the fourth silicon energy loss vs. the third.

plot. Si 2 dE is the y-axis on the middle plot and the x-axis on the right-most plot. Si 3 dE is the y-axis on the right-most plot.

In the leftmost panels of the top and bottom rows in Fig. 5, the first silicon detector (Si 0) registered roughly the same energy loss for all events. The spread is introduced by the energy spread of the beam and the resolution of the detector itself. The dE measurement from Si 1 separates events into two distinguishable groups. Events in the upper group on the 2D spectrum (red-highlighted peak in the 1D spectrum) lose more energy in Si 1 because no proton knockout occurred between the two detectors. There are three clusters in the middle panel corresponding to unreacted $^{27}\mathrm{F}$ (top), oxygen reaction products from Be 1 (bottom left) and oxygen reaction products from Be 2 (bottom right); the two lower clusters both contribute to the blue-highlighted peak on the left of the "Si 2 dE" 1D spectrum. The two groups in the right-bottom panel correspond to oxygen reaction products from Be 1 or Be 2 (left) and oxygen reaction products from Be 3 (right).

4. Results and discussion

4.1. Monte Carlo simulation of $^{26}\mathrm{O} \rightarrow {}^{24}\mathrm{O} + 2n$

To illustrate the effect that the target thickness has on the decay energy resolution, the reaction $^{27}\mathrm{F}(-1p) \rightarrow {}^{26}\mathrm{O} \rightarrow {}^{24}\mathrm{O} + 2n$ was simulated to model the reaction mechanism and the decay process as well as the detector responses. The simulation output has the same format as the calibrated data, so it is processed through the same decay energy calculation that is used for the experimental data. The resulting spectrum has the detector acceptances, efficiencies and resolutions folded in so it is directly comparable to the experimental data. The simulation also outputs the neutron kinematic quantities before they are processed to simulate the detector response so that the target thickness effects can be separated from the response of the neutron detectors.

The right panel in Fig. 6 compares four decay energy spectra reconstructed from simulations of a single thick (11.1 mm) beryllium target

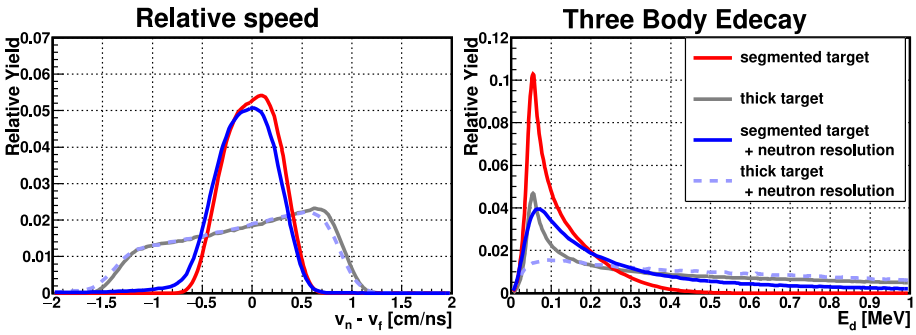

Fig. 6. Results from a simulation run with a single 11.1 mm target (gray and blue dashed curves) and with a segmented target (red and solid blue curves). The 11.1 mm target is the sum of the thicknesses of the three beryllium targets used in the segmented target described here. For the segmented target simulation, the detector and target thicknesses in the simulation are the same as those listed in Table 1. The left panel plots the difference in speed $|\vec{v}_n| - |\vec{v}_f|$ between one neutron and the charged fragment. The right panel plots the three body decay energy calculated from the simulation outputs for the fragment and both neutrons. For the red and gray curves, the neutron four-vectors were calculated from the simulated kinematic quantities and not from the results of the detector response modeling. The solid-blue and dashed-blue curves show the relative speed and decay energy distributions when the neutron detector response is included. (For interpretation of the references to color in this figure legend, the reader is referred to the web version of this article.)

without (gray line) and including (blue dashed line) the response of the neutron detectors. Note that the 11.1 mm represents the sum of the thicknesses of the three targets used in the experiment here. For these simulations, 488.7 MeV was added to the ^{24}O kinetic energy measured after the target in order to approximate the kinetic energy at the decay vertex, assumed to be at the center of the target. This will be referred to as a thick target reconstruction. The red curve shows the result for a simulation with a segmented target consisting of three separate pieces of beryllium 4.1 mm, 3.7 mm and 3.3 mm thick, see Table 1. The blue curve plots the result from a segmented target simulation that incorporated the response of the neutron detectors. In these simulations, the energy losses measured by the silicon detectors were analyzed to determine in which beryllium section the reaction occurred, as described in Section 3.2. Based on this determination, one of the three values listed in Table 4 was added to the fragment kinetic energy measured after the segmented target stack. This will be referred to as a segmented target reconstruction.

The input decay energy for every event in all simulations was 50 keV. For both the red and the gray lines, the reconstructed decay energies are broadened relative to the input distribution because of the uncertainty in the reaction/decay location within the target. The response of the neutron detectors was simulated using GEANT4 [23] and a custom neutron interaction package [24] to model neutron interactions in the MoNA/LISA scintillator bars. The resolution was simulated by adding Gaussian distributed noise ($\sigma = 0.2$ ns) to the time-of-flight values and to the x position ($\sigma = 3$ cm). The discretization in y and z due to the physical locations of the bars is also reproduced in the GEANT simulation. Including the detector response/resolution further degrades the resolution of the decay energy spectrum. Note that a peak is no longer discernible in the thick target case (dashed line).

The left panel in Fig. 6 compares the neutron-fragment relative speed distributions for the thick (gray curve) and segmented (red curve) target simulations. The solid dark blue and dashed light blue curves correspond to segmented and thick simulations, respectively, that include the response of the neutron detectors as discussed in the previous paragraph. The relative speed is calculated as $|\vec{v}_n| - |\vec{v}_f|$ where $v_f = v_0 + v_{\text{const}}$; $v_{\text{const}} \propto \sqrt{E_{\text{const}}}$ represents the adjustment (due to the thick or segmented target reconstruction) to the measured velocity v_0. For the low decay energy case simulated here, the lab frame neutron and fragment velocities are similar to the beam velocity at the decay vertex. After the decay the fragment travels through the remainder of the target material and loses energy. The thick and segmented target reconstructions serve to account for this energy loss and recover the kinetic energy at the vertex. Since the average reaction/decay position is the center of the target, the event-by-event energy loss is estimated as the energy lost by a fragment produced at the center of the target.

Table 4
Energy loss estimate used to reconstruct the energy of the ^{24}O fragments produced when ^{27}F interacts with one of the ^{9}Be targets.

Target	Energy loss estimate [MeV]
Be 1	785.0
Be 2	488.7
Be 3	177.6

The deviation from zero of the relative speed distribution's centroid quantifies how well this estimate reproduces the event-by-event actual energy loss. The width of the relative speed distribution is related to the thickness of the target and the decay energy of the unbound resonance. At a fixed decay energy, a thicker target results in a larger spread of reaction/decay points around the target center and translates to a larger spread of actual energy losses around the estimated value. This introduces a spread in the relative speed proportional to the target thickness as illustrated by the difference between the gray and red curves (and the solid and dashed blue curves) in the left panel of Fig. 6.

4.2. Improved decay energy resolution

Data from a recent measurement carried out by the MoNA Collaboration at the NSCL formed the basis to evaluate the performance of the segmented target [19]. Two-neutron unbound ^{26}O was populated via one proton knockout from ^{27}F. This nucleus has been previously measured at various facilities [25,26] and two resonances have been identified [27]. Fig. 7 shows the relative speed and three-body decay-energy spectra reconstructed from data (points) and simulation (lines). In the simulation, the decay of the ^{26}O ground state was modeled as a simultaneous emission of two uncorrelated neutrons for which the decay energy distribution was a delta function at 50 keV. Other decay channels, like the decay of the 1.28 MeV excited state in ^{26}O, are considered background. These processes are modeled as a two-neutron sequential decay from ^{26}O in which the allowed decay energies are uniformly distributed between 50 and 450 keV for one neutron emission and uniformly between 600 and 800 keV for the other neutron emission.

In the top row of Fig. 7, the segmented target reconstruction procedure was used to select one of the three energy loss estimates listed in Table 4. The plots in the bottom row of Fig. 7 were produced from the thick target reconstruction where the energy loss estimate for the second beryllium target (see Table 4) was used for all events. Just as in the simulated case (Fig. 6) there is a substantial improvement in the decay energy resolution of the segmented target spectrum compared to the single thick target reconstruction.

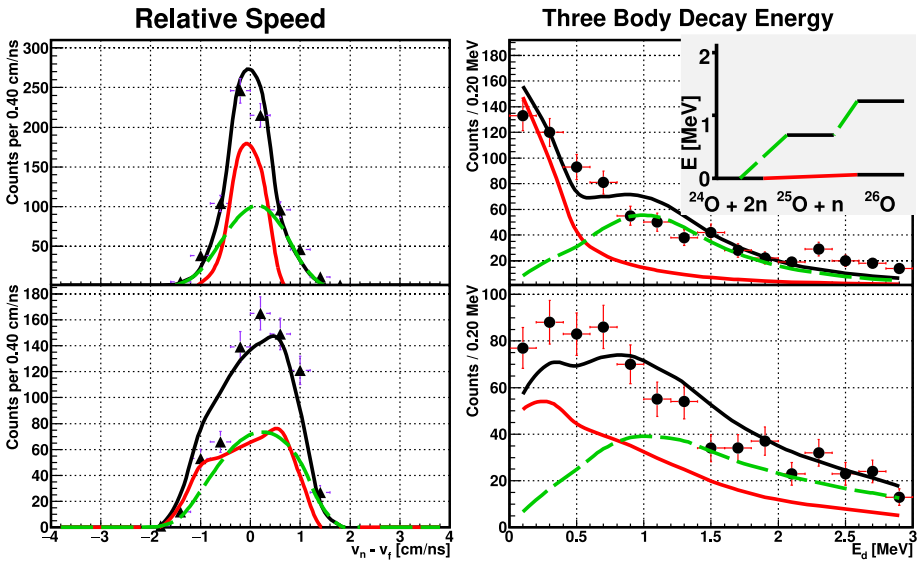

Fig. 7. Measured relative speed and three body decay energy spectra for ^{27}F($-1p$) → ^{26}O → ^{24}O + 2n are drawn as black triangles and black circles, respectively. The solid curves are spectra reconstructed from simulation. Two different decay channels were simulated (see inset of top right panel): (1) direct population of the ^{26}O ground state followed by two-neutron emission (red solid line) and (2) population of the ^{26}O first excited state followed by a sequential neutron emission through the ^{25}O ground state (green dashed line). In the top row, the segmented target reconstruction procedure is followed. In the bottom row, the energy loss estimate for the middle beryllium segment is applied to all events.

As mentioned above, the spread of the relative speed distribution is related to the target thickness and to the decay energy that is partitioned among the fragment and neutrons. When more energy is available in the decay the difference between the momenta of the daughter products will be larger. This is why the upper and lower tails (e.g. the upper left panel in Fig. 7) of the relative speed distribution correspond to higher decay energies (see also Eq. (2)). For low decay energies, like the ^{26}O ground state, a large mismatch between the actual fragment energy loss and the estimated value results in artificially high decay energies; note the much larger tail on the low energy peak in the bottom right panel compared to the upper right in Fig. 7.

4.3. Data-statistics

In cases where one needs to discriminate between two decay channels like the ones shown in Fig. 7, the improved resolution offered by the segmented target allows for a cleaner gate on the three body decay energy which provides better statistics for studies of a single unbound resonance. For the case of the ^{26}O ground state, there are two sources of background in the ^{24}O + 2n data set: (1) cross-talk events in which the two hits in MoNA/LISA are the result of a single neutron interacting in two separate locations and (2) events in which the decay of some other state was observed. Background of the first type is suppressed by requiring a spatial (25 cm) and velocity (7 cm/ns) separation between two interactions, following the description given in [25,28,29]. Background of the second type is suppressed by selecting events in which the three body decay energy is less than 300 keV, see Fig. 7. An additional 31 events fall below the 300 keV decay energy cut when the segmented target reconstruction method is used instead of the thick target reconstruction (see Fig. 9).

Another objective of the aforementioned experiment was to study the half-life of the ^{26}O ground state. The signature of a measurable ($T_{1/2} \sim 1$ ps) half-life is a shift in the relative speed distribution. This technique was applied to data from the MoNA Collaboration's first measurement of ^{26}O and the results were reported in Ref. [30]. The principle is illustrated in Fig. 8 and described in detail in Ref. [31]. If the decay of ^{26}O does not occur instantaneously, then the nucleus will slow down as it travels through the target material. As a result, the

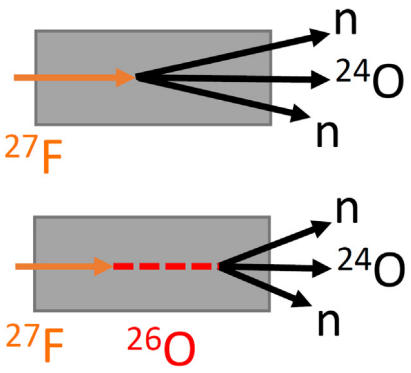

Fig. 8. An illustration of the decay in target technique. The longer ^{26}O exists ($T_{1/2} \sim 10^{-12}$ s, bottom panel), the more energy it loses as it travels through the target material. This means the neutrons are emitted with a lower velocity than if ^{26}O decays instantaneously ($T_{1/2} \sim 10^{-21}$ s, top panel).

neutrons are emitted with a slower speed than if the decay happens instantaneously. This shifts the centroid of the relative speed distribution below zero.

In order to extract a half-life ($T_{1/2}$) for ^{26}O, the simulation was modified to account for the delayed neutron emission. After the proton knockout occurs at some random position inside the target, the simulation propagates the ^{26}O for an amount of time randomly drawn from an exponential distribution before the decay to ^{24}O + n + n is simulated. Relative speed distributions simulated with $T_{1/2}$ = 0, 4 and 8 ps are shown as the curves in the upper left panel of Fig. 9. For consistency with the previous analysis [30], an unbinned maximum likelihood technique [32] was used to extract the statistical uncertainties.

The systematic uncertainty was estimated by examining the decay of the first unbound excited state of ^{23}O* → ^{22}O + n [33]. Since the half-life for this decay is ~10^{-18} s, the relative speed distribution should not be shifted away from zero, see Fig. 10. This decay was measured at the same time as ^{26}O with an identical setup: segmented target, magnet setting, MoNA configuration, Sweeper detector settings and calibrations. The same half-life analysis described in the previous

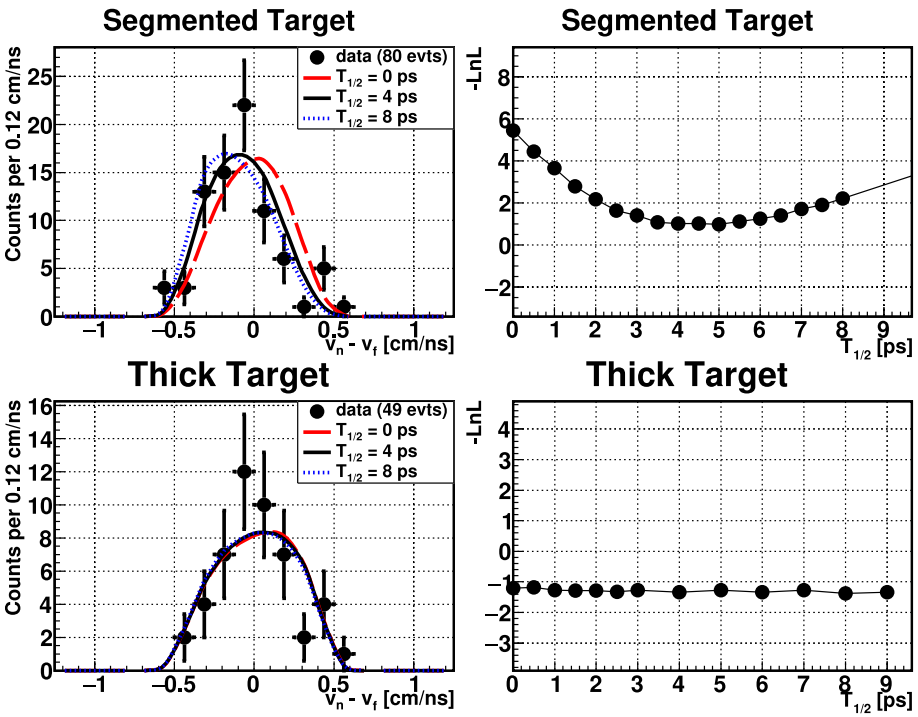

Fig. 9. The top left plot shows the relative speed distribution resulting from the segmented target reconstruction (see Sections 3.2 and 4.2). The black points are data and the curves represent relative speed distributions simulated assuming various $T_{1/2}$ for ^{26}O — red dashed is 0 ps, black solid is 4 ps and blue dotted corresponds to 8 ps. In the bottom left the thick target reconstruction procedure is followed. The right panels show the extracted negative loglikelihood curves for the segmented (top) and single thick (bottom) target reconstructions.

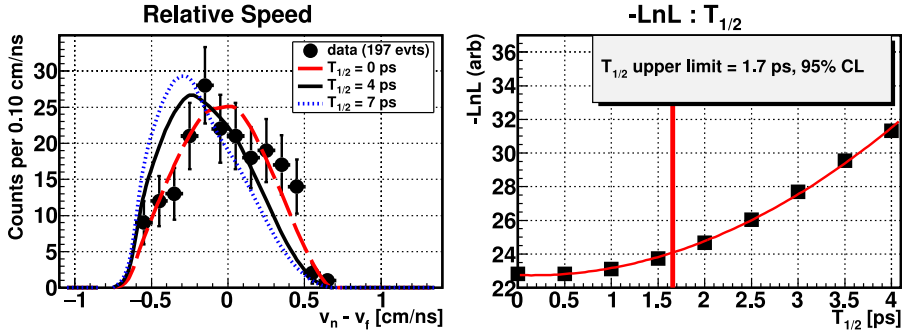

Fig. 10. Half-life extracted from $^{23}O^* \rightarrow {}^{22}O + n$ data taken during the ^{26}O measurement. The left panel shows the relative speed distribution for data (black points) and three simulations with $T_{1/2} = 0$ ps, 4 ps, and 7 ps. The right panel shows the negative loglikelihood as a function of half-life. The red vertical line indicates the 1.7 ps upper limit corresponding to a 95% confidence level.

paragraph was used to extract an upper limit for the $^{23}O^*$ decay in order to quantify how accurately the experimental setup and the analysis can measure a known $T_{1/2} = 0$. The upper limit on the $^{23}O^*$ half-life was found to be 1.7 ps with a 95% confidence level. Including the 1σ statistical uncertainties, the half-life of the ^{26}O ground state was found to be $T_{1/2} = 5^{+1.7}_{-2.2}$ (stat)±1.7 (syst) ps.

The result extracted from this new measurement agrees with the results of Ref. [30]. Even with the detector malfunction mentioned in Section 2.4, increased statistics afforded by an effectively thicker target compensated for a reduction in charged-particle detection efficiency. Good decay energy resolution due to target segmentation allowed ^{26}O ground state decays to be separated from background events achieving a sensitivity to the half-life. The bottom row in Fig. 9 shows that reconstructing the fragment momentum without accounting for the target segmentation destroys the half-life sensitivity because of the reduced resolution discussed above.

The resolution of the neutron detectors will also broaden the relative speed distribution and decrease the sensitivity of the half-life measurement. In order to examine this effect, two pseudo data sets were generated from the $T_{1/2} = 5$ ps segmented target simulation by randomly selecting 100 events from before and after folding in the neutron detector response. The relative speed distributions for these pseudo data sets were analyzed in the same way as the data and the negative loglikelihood curves shown in Fig. 11 were extracted. The 1σ confidence interval for the pseudo data set with the detector response included is 4 ps wide while the corresponding interval without the detector response is 2.4 ps. Therefore the sensitivity of this method could be improved by no more than a factor of 1.7 through improvements in the neutron detector response.

5. Conclusion

In summary, a new device was developed for use in invariant mass spectroscopy of neutron unbound states at the NSCL. It consists of three beryllium targets interleaved with four silicon detectors. The energy

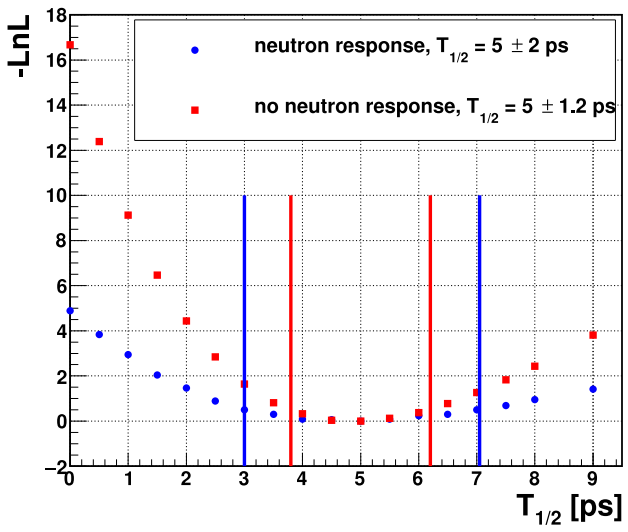

Fig. 11. The impact of the neutron detector response on the extracted half-life is compared using two pseudo data sets. The blue circles plot the negative loglikelihood for the pseudo data set that includes the detector response and the red squares show the result without the detector response. The blue (red) vertical lines indicate the 1σ confidence intervals for the pseudo data sets with (without) the detector response. (For interpretation of the references to color in this figure legend, the reader is referred to the web version of this article.)

loss measured in each silicon allows the reaction that produces the unbound state to be localized to a particular beryllium segment. This improves the accuracy of the energy loss estimate used to reconstruct the fragment momentum. The result is an effectively thicker reaction target for improved reaction yield without sacrificing decay energy resolution.

The segmented target was commissioned during an experiment to measure the half-life of ^{26}O. Two versions of the analysis were conducted: (1) a single target equal in thickness to the sum of the three beryllium segments was assumed when reconstructing the fragment momentum and (2) the dE measurements were used to identify the target segment containing the reaction and the estimate for that particular segment was applied. Method (2) results in a better reconstruction of the fragment momentum. Consequently, the relative speed and decay energy resolutions were much improved in method (2) compared to method (1) allowing the half-life of the ^{26}O ground state to be extracted.

CRediT authorship contribution statement

T. Redpath: Methodology, Software, Validation, Formal analysis, Investigation, Data curation, Writing - original draft, Writing - review & editing, Visualization. **T. Baumann:** Conceptualization, Methodology, Investigation, Resources, Writing - review & editing, Supervision. **J. Brown:** Conceptualization, Methodology, Investigation, Resources. **D. Chrisman:** Investigation. **P.A. DeYoung:** Conceptualization, Methodology, Investigation, Resources, Writing - review & editing, Supervision. **N. Frank:** Conceptualization, Methodology, Investigation, Resources, Writing - review & editing, Supervision. **P. Guèye:** Conceptualization, Investigation, Resources, Writing - review & editing. **A.N. Kuchera:** Investigation, Writing - review & editing, Supervision. **H. Liu:** Investigation. **C. Persch:** Investigation, Data curation, Visualization. **S. Stephenson:** Conceptualization, Investigation, Writing - review & editing, Supervision. **K. Stiefel:** Investigation. **M. Thoennessen:** Conceptualization, Methodology, Investigation, Resources, Data curation, Writing - review & editing, Supervision, Project administration, Funding acquisition. **D. Votaw:** Investigation, Software, Formal analysis.

Declaration of competing interest

The authors declare that they have no known competing financial interests or personal relationships that could have appeared to influence the work reported in this paper.

Acknowledgments

This work was supported by the National Science Foundation, USA under Grants No. PHY-1102511, PHY-1565546, PHY-1613188, PHY-1713522, PHY-1613429, PHY-1713956. This work was also supported by the Department of Energy National Nuclear Security Administration, USA through the Nuclear Science and Security Consortium under Award No. DE-NA0003180.

References

[1] R.J. Charity, K.W. Brown, J. Elson, W. Reviol, L.G. Sobotka, W.W. Buhro, Z. Chajecki, W.G. Lynch, J. Manfredi, R. Shane, R.H. Showalter, M.B. Tsang, D. Weisshaar, J. Winkelbauer, S. Bedoor, D.G. McNeel, A.H. Wuosmaa, Invariant-mass spectroscopy of ^{18}Ne,^{16} O, and ^{10}C excited states formed in neutron-transfer reactions, Phys. Rev. C 99 (2019) 044304, http://dx.doi.org/10.1103/PhysRevC.99.044304.

[2] R.J. Charity, K.W. Brown, J. Okołowicz, M. Płoszajczak, J.M. Elson, W. Reviol, L.G. Sobotka, W.W. Buhro, Z. Chajecki, W.G. Lynch, J. Manfredi, R. Shane, R.H. Showalter, M.B. Tsang, D. Weisshaar, J.R. Winkelbauer, S. Bedoor, A.H. Wuosmaa, Invariant-mass spectroscopy of ^{14}O excited states, Phys. Rev. C 100 (2019) 064305, http://dx.doi.org/10.1103/PhysRevC.100.064305.

[3] T. Baumann, A. Spyrou, M. Thoennessen, Nuclear structure experiments along the neutron drip line, Rep. Progr. Phys. 75 (3) (2012) 036301, http://dx.doi.org/10.1088/0034-4885/75/3/036301.

[4] M.D. Jones, T. Baumann, J. Brett, J. Bullaro, P.A. DeYoung, J.E. Finck, N. Frank, K. Hammerton, J. Hinnefeld, Z. Kohley, A.N. Kuchera, J. Pereira, A. Rabeh, J.K. Smith, A. Spyrou, S.L. Stephenson, K. Stiefel, M. Tuttle-Timm, R.G.T. Zegers, M. Thoennessen, Neutron-unbound excited states of ^{23}N, Phys. Rev. C 95 (2017) 044323, http://dx.doi.org/10.1103/PhysRevC.95.044323.

[5] J. Hwang, S. Kim, Y. Satou, N. Orr, Y. Kondo, T. Nakamura, J. Gibelin, N. Achouri, T. Aumann, H. Baba, F. Delaunay, P. Doornenbal, N. Fukuda, N. Inabe, T. Isobe, D. Kameda, D. Kanno, N. Kobayashi, T. Kobayashi, T. Kubo, S. Leblond, J. Lee, F. Marqués, R. Minakata, T. Motobayashi, D. Murai, T. Murakami, K. Muto, T. Nakashima, N. Nakatsuka, A. Navin, S. Nishi, S. Ogoshi, H. Otsu, H. Sato, Y. Shimizu, H. Suzuki, K. Takahashi, H. Takeda, S. Takeuchi, R. Tanaka, Y. Togano, A. Tuff, M. Vandebrouck, K. Yoneda, Single-neutron knockout from ^{20}C and the structure of ^{19}C, Phys. Lett. B 769 (2017) 503–508, http://dx.doi.org/10.1016/j.physletb.2017.04.019, URL http://www.sciencedirect.com/science/article/pii/S0370269317302939.

[6] M. Vandebrouck, A. Lepailleur, O. Sorlin, T. Aumann, C. Caesar, M. Holl, V. Panin, F. Wamers, S.R. Stroberg, J.D. Holt, F. de Oliveira Santos, H. Alvarez-Pol, L. Atar, V. Avdeichikov, S. Beceiro-Novo, D. Bemmerer, J. Benlliure, C.A. Bertulani, S.K. Bogner, J.M. Boillos, K. Boretzky, M.J.G. Borge, M. Caamaño, E. Casarejos, W. Catford, J. Cederkäll, M. Chartier, L. Chulkov, D. Cortina-Gil, E. Cravo, R. Crespo, U. Datta Pramanik, P. Díaz Fernández, I. Dillmann, Z. Elekes, J. Enders, O. Ershova, A. Estradé, F. Farinon, L.M. Fraile, M. Freer, D. Galaviz, H. Geissel, R. Gernhäuser, J. Gibelin, P. Golubev, K. Göbel, J. Hagdahl, T. Heftrich, M. Heil, M. Heine, A. Heinz, A. Henriques, H. Hergert, A. Hufnagel, A. Ignatov, H.T. Johansson, B. Jonson, J. Kahlbow, N. Kalantar-Nayestanaki, R. Kanungo, A. Kelic-Heil, A. Knyazev, T. Kröll, N. Kurz, M. Labiche, C. Langer, T. Le Bleis, R. Lemmon, S. Lindberg, J. Machado, J. Marganiec, F.M. Marqués, A. Movsesyan, E. Nacher, M. Najafi, E. Nikolskii, T. Nilsson, C. Nociforo, S. Paschalis, A. Perea, M. Petri, S. Pietri, R. Plag, R. Reifarth, G. Ribeiro, C. Rigollet, M. Röder, D. Rossi, D. Savran, H. Scheit, A. Schwenk, H. Simon, I. Syndikus, J.T. Taylor, O. Tengblad, R. Thies, Y. Togano, P. Velho, V. Volkov, A. Wagner, H. Weick, C. Wheldon, G. Wilson, J.S. Winfield, P. Woods, D. Yakorev, M. Zhukov, A. Zilges, K. Zuber, Effective proton–neutron interaction near the drip line from unbound states in ^{25,26}F, Phys. Rev. C 96 (2017) 054305, http://dx.doi.org/10.1103/PhysRevC.96.054305.

[7] J.K. Smith, T. Baumann, D. Bazin, J. Brown, S. Casarotto, P.A. DeYoung, N. Frank, J. Hinnefeld, M. Hoffman, M.D. Jones, Z. Kohley, B. Luther, B. Marks, N. Smith, J. Snyder, A. Spyrou, S.L. Stephenson, M. Thoennessen, N. Viscariello, S.J. Williams, Low-lying neutron unbound states in ^{12}Be, Phys. Rev. C 90 (2014) 024309, http://dx.doi.org/10.1103/PhysRevC.90.024309.

[8] G. Christian, N. Frank, S. Ash, T. Baumann, D. Bazin, J. Brown, P.A. Deyoung, J.E. Finck, A. Gade, G.F. Grinyer, A. Grovom, J.D. Hinnefeld, E.M. Lunderberg, B. Luther, M. Mosby, S. Mosby, T. Nagi, G.F. Peaslee, W.F. Rogers, J.K. Smith, J. Snyder, A. Spyrou, M.J. Strongman, M. Thoennessen, M. Warren, D. Weisshaar, A. Wersal, Exploring the low-Z shore of the Island of inversion at N=19, Phys. Rev. Lett. 108 (3) (2012) 1–5, http://dx.doi.org/10.1103/PhysRevLett.108.032501.

[9] S. Leblond, F.M. Marqués, J. Gibelin, N.A. Orr, Y. Kondo, T. Nakamura, J. Bonnard, N. Michel, N.L. Achouri, T. Aumann, H. Baba, F. Delaunay, Q. Deshayes, P. Doornenbal, N. Fukuda, J.W. Hwang, N. Inabe, T. Isobe, D. Kameda, D. Kanno, S. Kim, N. Kobayashi, T. Kobayashi, T. Kubo, J. Lee, R. Minakata, T. Motobayashi, D. Murai, T. Murakami, K. Muto, T. Nakashima, N. Nakatsuka, A. Navin, S. Nishi, S. Ogoshi, H. Otsu, H. Sato, Y. Satou, Y. Shimizu, H. Suzuki, K. Takahashi, H. Takeda, S. Takeuchi, R. Tanaka, Y. Togano, A.G. Tuff, M. Vandebrouck, K. Yoneda, First observation of ^{20}B and ^{21}B, Phys. Rev. Lett. 121 (2018) 262502, http://dx.doi.org/10.1103/PhysRevLett.121.262502.

[10] Y. Ayyad, N. Abgrall, T. Ahn, H. Álvarez Pol, D. Bazin, S. Beceiro-Novo, L. Carpenter, R. Cooper, M. Cortesi, A. Macchiavelli, W. Mittig, B. Olaizola, J. Randhawa, C. Santamaria, N. Watwood, J. Zamora, R. Zegers, Next-generation experiments with the active target time projection chamber (at-tpc), Nucl. Instrum. Methods Phys. Res. A. http://dx.doi.org/10.1016/j.nima.2018.10.019. URL http://www.sciencedirect.com/science/article/pii/S0168900218313342.

[11] T. Furuno, T. Kawabata, H. Ong, S. Adachi, Y. Ayyad, T. Baba, Y. Fujikawa, T. Hashimoto, K. Inaba, Y. Ishii, S. Kabuki, H. Kubo, Y. Matsuda, Y. Matsuoka, T. Mizumoto, T. Morimoto, M. Murata, T. Sawano, T. Suzuki, A. Takada, J. Tanaka, I. Tanihata, T. Tanimori, D. Tran, M. Tsumura, H. Watanabe, Performance test of the maiko active target, Nucl. Instrum. Methods Phys. Res. A 908 (2018) 215–224, http://dx.doi.org/10.1016/j.nima.2018.08.042, URL http://www.sciencedirect.com/science/article/pii/S0168900218309951.

[12] A. Laird, P. Amaudruz, L. Buchmann, S. Fox, B. Fulton, D. Gigliotti, T. Kirchner, P. Mumby-Croft, R. Openshaw, M. Pavan, J. Pearson, G. Ruprecht, G. Sheffer, P. Walden, Status of tactic: A detector for nuclear astrophysics, in: Proceedings of the 7th International Conference on Position-Sensitive Detectors, Nucl. Instrum. Methods Phys. Res. A 573 (1) (2007) 306–309, http://dx.doi.org/10.1016/j.nima.2006.10.384, URL http://www.sciencedirect.com/science/article/pii/S0168900206021553.

[13] S. Beceiro-Novo, T. Ahn, D. Bazin, W. Mittig, Active targets for the study of nuclei far from stability, Prog. Part. Nucl. Phys. 84 (2015) 124–165, http://dx.doi.org/10.1016/j.ppnp.2015.06.003, URL http://www.sciencedirect.com/science/article/pii/S0146641015000459.

[14] A. Banu, Y. Li, M. McCleskey, M. Bullough, S. Walsh, C. Gagliardi, L. Trache, R. Tribble, C. Wilburn, Performance evaluation of position-sensitive silicon detectors with four-corner readout, Nucl. Instrum. Methods Phys. Res. A. http://dx.doi.org/10.1016/j.nima.2008.05.016.

[15] NSCL, National superconducting cyclotron laboratory, 2019, https://www.nscl.msu.edu/.

[16] T. Baumann, J. Boike, J. Brown, M. Bullinger, J.P. Bychoswki, S. Clark, K. Daum, P.A. Deyoung, J.V. Evans, J. Finck, N. Frank, A. Grant, J. Hinnefeld, G.W. Hitt, R.H. Howes, B. Isselhardt, K.W. Kemper, J. Longacre, Y. Lu, B. Luther, S.T. Marley, D. McCollum, E. McDonald, U. Onwuemene, P.V. Pancella, G.F. Peaslee, W.A. Peters, M. Rajabali, J. Robertson, W.F. Rogers, S.L. Tabor, M. Thoennessen, E. Tryggestad, R.E. Turner, P.J. Vanwylen, N. Walker, Construction of a modular large-area neutron detector for the NSCL, Nucl. Instrum. Methods Phys. Res. A 543 (2–3) (2005) 517–527, http://dx.doi.org/10.1016/j.nima.2004.12.020.

[17] B. Luther, T. Baumann, M. Thoennessen, J. Brown, P. DeYoung, J. Finck, J. Hinnefeld, R. Howes, K. Kemper, P. Pancella, G. Peaslee, W. Rogers, S. Tabor, Mona - the modular neutron array, in: Proceedings of the Tenth Symposium on Radiation Measurements and Applications, Nucl. Instrum. Methods Phys. Res. A 505 (1) (2003) 33–35, http://dx.doi.org/10.1016/S0168-9002(03)01014-3, URL http://www.sciencedirect.com/science/article/pii/S0168900203010143.

[18] M.D. Bird, S.J. Kenney, J. Toth, H.W. Weijers, J.C. DeKamp, M. Thoennessen, A.F. Zeller, System testing and installation of the NHMFL/NSCL sweeper magnet, IEEE Trans. Appl. Supercond. 15 (2 PART II) (2005) 1252–1254, http://dx.doi.org/10.1109/TASC.2005.849553.

[19] T. Redpath, Measuring the Half-Life of O-26 (Ph.D. thesis), Michigan State University, 2019.

[20] F. Marti, P. Miller, D. Poe, M. Steiner, J. Stetson, X.Y. Wu, Commissioning of the coupled cyclotron system at nscl, AIP Conf. Proc. 600 (1) (2001) 64–68, http://dx.doi.org/10.1063/1.1435199.

[21] D.J. Morrissey, B.M. Sherrill, M. Steiner, A. Stolz, I. Wiedenhoever, Commissioning the A1900 projectile fragment separator, Nucl. Instrum. Methods Phys. Res. 204 (2003) 90–96, http://dx.doi.org/10.1016/S0168-583X(02)01895-5.

[22] O.B. Tarasov, D. Bazin, LISE++: Radioactive beam production with in-flight separators, Nucl. Instrum. Methods Phys. Res. B 266 (19–20) (2008) 4657–4664, http://dx.doi.org/10.1016/j.nimb.2008.05.110.

[23] S. Agostinelli, J. Allison, K. Amako, J. Apostolakis, H. Araujo, P. Arce, M. Asai, D. Axen, S. Banerjee, G. Barrand, F. Behner, L. Bellagamba, J. Boudreau, L. Broglia, A. Brunengo, H. Burkhardt, S. Chauvie, J. Chuma, R. Chytracek, G. Cooperman, G. Cosmo, P. Degtyarenko, A. Dell'Acqua, G. Depaola, D. Dietrich, R. Enami, A. Feliciello, C. Ferguson, H. Fesefeldt, G. Folger, F. Foppiano, A. Forti, S. Garelli, S. Giani, R. Giannitrapani, D. Gibin, J.G. Cadenas, I. González, G.G. Abril, G. Greeniaus, W. Greiner, V. Grichine, A. Grossheim, S. Guatelli, P. Gumplinger, R. Hamatsu, K. Hashimoto, H. Hasui, A. Heikkinen, A. Howard, V. Ivanchenko, A. Johnson, F. Jones, J. Kallenbach, N. Kanaya, M. Kawabata, Y. Kawabata, M. Kawaguti, S. Kelner, P. Kent, A. Kimura, T. Kodama, R. Kokoulin, M. Kossov, H. Kurashige, E. Lamanna, T. Lampén, V. Lara, V. Lefebure, F. Lei, M. Liendl, W. Lockman, F. Longo, S. Magni, M. Maire, E. Medernach, K. Minamimoto, P.M. de Freitas, Y. Morita, K. Murakami, M. Nagamatu, R. Nartallo, P. Nieminen, T. Nishimura, K. Ohtsubo, M. Okamura, S. O'Neale, Y. Oohata, K. Paech, J. Perl, A. Pfeiffer, M. Pia, F. Ranjard, A. Rybin, S. Sadilov, E.D. Salvo, G. Santin, T. Sasaki, N. Savvas, Y. Sawada, S. Scherer, S. Sei, V. Sirotenko, D. Smith, N. Starkov, H. Stoecker, J. Sulkimo, M. Takahata, S. Tanaka, E. Tcherniaev, E.S. Tehrani, M. Tropeano, P. Truscott, H. Uno, L. Urban, P. Urban, M. Verderi, A. Walkden, W. Wander, H. Weber, J. Wellisch, T. Wenaus, D. Williams, D. Wright, T. Yamada, H. Yoshida, D. Zschiesche, Geant4—a simulation toolkit, Nucl. Instrum. Methods Phys. Res. A 506 (3) (2003) 250–303, http://dx.doi.org/10.1016/S0168-9002(03)01368-8, URL http://www.sciencedirect.com/science/article/pii/S0168900203013688.

[24] Z. Kohley, E. Lunderberg, P. DeYoung, B. Roeder, T. Baumann, G. Christian, S. Mosby, J. Smith, J. Snyder, A. Spyrou, M. Thoennessen, Modeling interactions of intermediate-energy neutrons in a plastic scintillator array with geant4, Nucl. Instrum. Methods Phys. Res. A 682 (2012) 59–65, http://dx.doi.org/10.1016/j.nima.2012.04.060, URL http://www.sciencedirect.com/science/article/pii/S0168900212004329.

[25] E. Lunderberg, A. Schiller, A. Spyrou, D. Bazin, Z. Kohley, J. Snyder, B. Luther, M.J. Strongman, M. Thoennessen, A. Haagsma, J.E. Finck, G. Christian, P.A. DeYoung, H. Attanayake, T. Baumann, D. Divaratne, S. Mosby, S.M. Grimes, T. Nagi, G.F. Peaslee, N. Frank, Evidence for the ground-state resonance of O26, Phys. Rev. Lett. http://dx.doi.org/10.1103/physrevlett.108.142503.

[26] C. Caesar, J. Simonis, T. Adachi, Y. Aksyutina, J. Alcantara, S. Altstadt, H. Alvarez-Pol, N. Ashwood, T. Aumann, V. Avdeichikov, M. Barr, S. Beceiro, D. Bemmerer, J. Benlliure, C.A. Bertulani, K. Boretzky, M.J. Borge, G. Burgunder, M. Caamano, E. Casarejos, W. Catford, J. Cederkäll, S. Chakraborty, M. Chartier, L. Chulkov, D. Cortina-Gil, U. Datta Pramanik, P. Diaz Fernandez, I. Dillmann, Z. Elekes, J. Enders, O. Ershova, A. Estrade, F. Farinon, L.M. Fraile, M. Freer, M. Freudenberger, H.O. Fynbo, D. Galaviz, H. Geissel, R. Gernhäuser, P. Golubev, D. Gonzalez Diaz, J. Hagdahl, T. Heftrich, M. Heil, M. Heine, A. Heinz, A. Henriques, M. Holl, J.D. Holt, G. Ickert, A. Ignatov, B. Jakobsson, H.T. Johansson, B. Jonson, N. Kalantar-Nayestanaki, R. Kanungo, A. Kelic-Heil, R. Knöbel, T. Kröll, R. Krücken, J. Kurcewicz, M. Labiche, C. Langer, T. Le Bleis, R. Lemmon, O. Lepyoshkina, S. Lindberg, J. Machado, J. Marganiec, V. Maroussov, J. Menéndez, M. Mostazo, A. Movsesyan, A. Najafi, T. Nilsson, C. Nociforo, V. Panin, A. Perea, S. Pietri, R. Plag, A. Prochazka, A. Rahaman, G. Rastrepina, R. Reifarth, G. Ribeiro, M.V. Ricciardi, C. Rigollet, K. Riisager, M. Röder, D. Rossi, J. Sanchez Del Rio, D. Savran, H. Scheit, A. Schwenk, H. Simon, O. Sorlin, V. Stoica, B. Streicher, J. Taylor, O. Tengblad, S. Terashima, R. Thies, Y. Togano, E. Uberseder, J. Van De Walle, P. Velho, V. Volkov, A. Wagner, F. Wamers, H. Weick, M. Weigand, C. Wheldon, G. Wilson, C. Wimmer, J.S. Winfield, P. Woods, D. Yakorev, M.V. Zhukov, A. Zilges, M. Zoric, K. Zuber, Beyond the neutron drip line: The unbound oxygen isotopes 25O and 26O, Phys. Rev. C. http://dx.doi.org/10.1103/PhysRevC.88.034313. arXiv:1209.0156.

[27] Y. Kondo, J. Lee, S. Kim, A.G. Tuff, F. Delaunay, H. Baba, R. Minakata, D. Kanno, S. Ogoshi, S. Takeuchi, H. Sato, T. Nakamura, H. Takeda, P. Doornenbal, K. Yoneda, T. Aumann, N. Fukuda, H. Suzuki, D. Murai, J.W. Hwang, Y. Satou, S. Nishi, T. Kobayashi, M. Vandebrouck, T. Isobe, Y. Shimizu, F.M. Marqués, N. Inabe, T. Nakashima, T. Motobayashi, T. Kubo, A. Navin, K. Muto, N. Kobayashi, K. Takahashi, N.L. Achouri, N. Nakatsuka, S. Leblond, D. Kameda, T. Murakami, Y. Togano, N.A. Orr, H. Otsu, R. Tanaka, J. Gibelin, Nucleus O26 : A barely unbound system beyond the drip line, Phys. Rev. Lett. http://dx.doi.org/10.1103/physrevlett.116.102503.

[28] T. Nakamura, A.M. Vinodkumar, T. Sugimoto, N. Aoi, H. Baba, D. Bazin, N. Fukuda, T. Gomi, H. Hasegawa, N. Imai, M. Ishihara, T. Kobayashi, Y. Kondo, T. Kubo, M. Miura, T. Motobayashi, H. Otsu, A. Saito, H. Sakurai, S. Shimoura, K. Watanabe, Y.X. Watanabe, T. Yakushiji, Y. Yanagisawa, K. Yoneda, Observation of strong low-lying $e1$ strength in the two-neutron halo nucleus ^{11}Li, Phys. Rev. Lett. 96 (2006) 252502, http://dx.doi.org/10.1103/PhysRevLett.96.252502.

[29] C.R. Hoffman, T. Baumann, J. Brown, P.A. DeYoung, J.E. Finck, N. Frank, J.D. Hinnefeld, S. Mosby, W.A. Peters, W.F. Rogers, A. Schiller, J. Snyder, A. Spyrou, S.L. Tabor, M. Thoennessen, Observation of a two-neutron cascade from a resonance in ^{24}O, Phys. Rev. C 83 (2011) 031303, http://dx.doi.org/10.1103/PhysRevC.83.031303.

[30] Z. Kohley, T. Baumann, D. Bazin, G. Christian, P.A. Deyoung, J.E. Finck, N. Frank, M. Jones, E. Lunderberg, B. Luther, S. Mosby, T. Nagi, J.K. Smith, J. Snyder, A. Spyrou, M. Thoennessen, Study of two-neutron radioactivity in the decay of O26, Phys. Rev. Lett. http://dx.doi.org/10.1103/PhysRevLett.110.152501.

[31] M. Thoennessen, G. Christian, Z. Kohley, T. Baumann, M. Jones, J.K. Smith, J. Snyder, A. Spyrou, Novel techniques to search for neutron radioactivity, Nucl. Instrum. Methods Phys. Res. A. http://dx.doi.org/10.1016/j.nima.2013.07.035.

[32] D.M. Schmidt, R.J. Morrison, M.S. Witherell, A general method of estimating physical parameters from a distribution with acceptance and smearing effects, Nucl. Instrum. Methods Phys. Res. A 328 (3) (1993) 547–552, http://dx.doi.org/10.1016/0168-9002(93)90674-7.

[33] A. Schiller, N. Frank, T. Baumann, D. Bazin, B.A. Brown, J. Brown, P.A. DeYoung, J.E. Finck, A. Gade, J. Hinnefeld, R. Howes, J.-L. Lecouey, B. Luther, W.A. Peters, H. Scheit, M. Thoennessen, J.A. Tostevin, Selective population and neutron decay of an excited state of ^{23}O, Phys. Rev. Lett. 99 (2007) 112501, http://dx.doi.org/10.1103/PhysRevLett.99.112501.